

Characteristics of secondary electron emission from few layer graphene on silicon (111) surface

Guo-Bao Feng(封国宝), Yun Li(李韵), Xiao-Jun Li(李小军), Gui-Bai Xie(谢贵柏), and Lu Liu(刘璐)
Citation: Chin. Phys. B, 2022, 31 (**10**): 107901. DOI: 10.1088/1674-1056/ac76a9
Journal homepage: http://cpb.iphy.ac.cn; http://iopscience.iop.org/cpb

What follows is a list of articles you may be interested in

Effect of Cu doping on the secondary electron yield of carbon films on Ag-plated aluminum alloy

Tiancun Hu(胡天存), Shukai Zhu(朱淑凯), Yanan Zhao(赵亚楠), Xuan Sun(孙璇), Jing Yang(杨晶), Yun He(何鋆), Xinbo Wang(王新波), Chunjiang Bai(白春江), He Bai(白鹤), Huan Wei(魏焕), Meng Cao(曹猛), Zhongqiang Hu(胡忠强), Ming Liu(刘明), and Wanzhao Cui(崔万照)
Chin. Phys. B, 2022, 31 (**4**): 047901. DOI: 10.1088/1674-1056/ac322c

Secondary electron emission yield from vertical graphene nanosheets by helicon plasma deposition

Xue-Lian Jin(金雪莲), Pei-Yu Ji(季佩宇), Lan-Jian Zhuge(诸葛兰剑), Xue-Mei Wu(吴雪梅), and Cheng-Gang Jin(金成刚)
Chin. Phys. B, 2022, 31 (**2**): 027901. DOI: 10.1088/1674-1056/ac11dd

Analysis of secondary electron emission using the fractal method

Chun-Jiang Bai(白春江), Tian-Cun Hu(胡天存), Yun He(何鋆), Guang-Hui Miao(苗光辉), Rui Wang(王瑞), Na Zhang(张娜), and Wan-Zhao Cui(崔万照)
Chin. Phys. B, 2021, 30 (**1**): 017901. DOI: 10.1088/1674-1056/abc2be

Secondary electron yield suppression using millimeter-scale pillar array and explanation of the abnormal yield-energy curve

Ming Ye(叶鸣), Peng Feng(冯鹏), Dan Wang(王丹), Bai-Peng Song(宋佰鹏), Yong-Ning He(贺永宁), Wan-Zhao Cui(崔万照)
Chin. Phys. B, 2019, 28 (**7**): 077901. DOI: 10.1088/1674-1056/28/7/077901

Formula for average energy required to produce a secondary electron in an insulator

Xie Ai-Gen, Zhan Yu, Gao Zhi-Yong, Wu Hong-Yan
Chin. Phys. B, 2013, 22 (**5**): 057901. DOI: 10.1088/1674-1056/22/5/057901

Characteristics of secondary electron emission from few layer graphene on silicon (111) surface

Guo-Bao Feng(封国宝)[1], Yun Li(李韵)[1,†], Xiao-Jun Li(李小军)[1], Gui-Bai Xie(谢贵柏)[1], and Lu Liu(刘璐)[2]

[1] *National Key Laboratory of Science and Technology on Space Microwave, China Academy of Space Technology, Xi'an* 710100, *China*
[2] *School of Computer Science and Engineering, Xi'an University of Technology, Xi'an* 710048, *China*

(Received 31 March 2022; revised manuscript received 15 May 2022; accepted manuscript online 8 June 2022)

As a typical two-dimensional (2D) coating material, graphene has been utilized to effectively reduce secondary electron emission from the surface. Nevertheless, the microscopic mechanism and the dominant factor of secondary electron emission suppression remain controversial. Since traditional models rely on the data of experimental bulk properties which are scarcely appropriate to the 2D coating situation, this paper presents the first-principles-based numerical calculations of the electron interaction and emission process for monolayer and multilayer graphene on silicon (111) substrate. By using the anisotropic energy loss for the coating graphene, the electron transport process can be described more realistically. The real physical electron interactions, including the elastic scattering of electron–nucleus, inelastic scattering of the electron–extranuclear electron, and electron–phonon effect, are considered and calculated by using the Monte Carlo method. The energy level transition theory-based first-principles method and the full Penn algorithm are used to calculate the energy loss function during the inelastic scattering. Variations of the energy loss function and interface electron density differences for 1 to 4 layer graphene coating GoSi are calculated, and their inner electron distributions and secondary electron emissions are analyzed. Simulation results demonstrate that the dominant factor of the inhibiting of secondary electron yield (SEY) of GoSi is to induce the deeper electrons in the internal scattering process. In contrast, a low surface potential barrier due to the positive deviation of electron density difference at monolayer GoSi interface in turn weakens the suppression of secondary electron emission of the graphene layer. Only when the graphene layer number is 3, does the contribution of surface work function to the secondary electron emission suppression appear to be slightly positive.

Keywords: secondary electron emission, graphene on silicon, numerical simulation

PACS: 79.20.Hx, 81.05.ue, 78.20.Bh **DOI:** 10.1088/1674-1056/ac76a9

1. Introduction

Secondary electron emission from the material surface plays an essential role in multipactor,[1–4] which will seriously deteriorate the performances of spacecraft microwave components,[5–7] such as the fluctuation of cavity tuning, parameter coupling, waveguide loss, and phase constant, producing harmonics, leading to out-of-band interference and passive intermodulation products, and corroding the surface of components.[8–11] In recent years, since deep space exploration requires more miniaturization and high-power microwave components, the issue, *i.e.* the effective reduction of secondary electron emission and multipactor suppression, has become a significant challenge.[12–14] Nowadays, more attention has been focused on the surface coating treatment with a thin film, like low-dimensional carbon-based materials. In other fields, the studying of the electronic transport characteristics of 2D system heterostructures is also a critical topic, particularly the future application of these 2D materials in manufacturing microelectronic devices. Actually, considering that the integrated circuits keep miniaturizing on, physical limitations to effective carrier transport are experienced, such as secondary electron emission, which can dramatically hamper the performances of electronic devices. Furthermore, the investigation of interface formation for the reliable control of heteroboundary quality is of great significance in producing device-quality graphene with a realistic chance of entering into the market.

As a typical 2D material, graphene presents a remarkable inhibitory effect on secondary electron emission.[15–17] The graphene-coated microwave components can remarkably enhance the multipactor threshold when suffering high power and present a vast application prospect in several areas, ranging from scanning electron microscopy to spacecraft materials engineering to hadrontherapy. Nevertheless, owing to the lack of an integrated theoretical analysis method, the mechanism of suppressing the secondary electron emission of graphene is still under debate. By investigating the secondary electron emission of graphene on copper, Cao *et al.* thought that the suppression of graphene is mainly due to the greater considerable surface work function.[18] With statistically analyzing the correlations between the maximum values of secondary electron yield and surface work function of a variety of materials, Wang *et al.* found that a material with a lower work function always comes with a less secondary electron yield, which is mainly because most of conduction band electrons can be act as emitted secondary electrons.[19] Many researches mainly focused on surface geometric construction and adsorp-

[†]Corresponding author. E-mail: liy74@cast504.com, genliyun@126.com

© 2022 Chinese Physical Society and IOP Publishing Ltd

tion condition.[20,21] Actually, the secondary electron emission should be related to the effects of both inner scattering and surface work function. In theoretical research, although the classical formula, such as the Vaughan and Furman model, can satisfy the measurement results well,[22–24] those empirical formulas can hardly help reveal the physical mechanism from a microcosmic perspective. Monte Carlo simulation is the appropriate method for describing the micro-process of electrons inside the materials by considering elastic and inelastic scattering.[25–27] Mao *et al.*[28] and Penn *et al.*[29] introduced the dielectric loss of optical frequency to describe energy loss during electron–electron inelastic scattering. However, the critical optical constants, the extinction and refraction coefficients, rely on experiment data, making the micro-mechanism of secondary electron generation ambiguous, especially for 2D graphene-coated materials.[30] Without relying on experiment testing data, the first-principles calculation method can offer a practical method of obtaining the dielectric response characteristics of materials and the interface energy states of multilayer materials.[31–33] It can also offer a viable approach to figuring out the micro-mechanism of secondary electron emission from graphene.

In this work, to reveal the micro-mechanism for coating graphene to suppress secondary electron emission, we propose a numerical simulation method of the first-principles based on Monte Carlo to investigate the characteristics of secondary electron emission from the graphene on a silicon surface. Electrons inside material suffering elastic scattering are calculated with Mott scattering cross-section. The full Penn algorithm (FPA) is used to calculate the inelastic scattering, whose energy loss function is obtained by the first-principles simulation. We analyze the energy loss function from the electron energy level transition via the partial density of states (PDOS). Simulations by using this method are compared with experimental results from recent researches and our measurement system. One to four graphene layers are set on the silicon (111) surface to investigate suppression characteristics of secondary electron emission. Considering the Van der Waals' interaction between multilayer graphenes, the electron density differences between few-layer graphenes are analyzed. In addition, considering that the high conductivity graphene layer will remarkably change the dissipation form of internal deposited charge, we also analyze the internal charging states in different layers coating situations.

2. Simulation and measurement method

Incident primary electron will suffer a series of collisions with material atoms and the stimulation of outer shell electrons. Part of inner electrons can escape from the surface after traversing the surface potential to form secondary electrons (SE), while other parts will remain inside the dielectric, forming an internal charged states. Here, a series of inner electrons collisions is simulated with the Monte Carlo method, and the critical energy loss function is derived via the first-principles method. The secondary electron emission simulations are compared with recently reported results and experimental results in our measurement system.

2.1. Inner electron scattering

The scattering process can be divided into elastic scattering and inelastic scattering based on whether the collision of inner electrons comes with energy loss. The elastic scattering always happens between electrons and the atomic nucleus because the nuclear mass is much larger than the electron mass. The differential cross-section of elastic scattering $\mathrm{d}\sigma_\mathrm{e}(\theta)/\mathrm{d}\Omega$ can be calculated by using the Mott scattering model via incident partial wave function and scattering partial wave function.[34] The total scattering cross-section σ_Te can be obtained by integrating scattering angle θ between limits 0 and π as follows:

$$\sigma_\mathrm{Te} = \lambda_\mathrm{e}^{-1}/N = 2\pi \int_0^\pi [\mathrm{d}\sigma_\mathrm{e}(\theta)/\mathrm{d}\Omega] \sin\theta \,\mathrm{d}\theta, \tag{1}$$

where λ_e is the mean free path of elastic scattering in units of cm and N is the atom density in units of cm^{-3}.

For the inelastic scattering of energetic electron–electron interaction (apart from electron–phonon and electron–polaron), part of the energy will transform from energetic electron to extranuclear electron due to energy level transition or free electron excitation.

This energy loss process can be described via the dielectric function model. Then, Yan *et al.* developed an algorithm to derive this function from optical data,[35] which takes into consideration the energy loss $\hbar\omega$ and momentum conservation.

In this work, we use the full Penn algorithm (FPA) to derive the energy loss function.[36–38] Compared with the single pole approximation (SPA), the FPA considers both the single electron excitation and the plasmon excitation, making the Monte Carlo simulation of secondary electrons in a low energy range more accurate.

The energy loss per length $-\mathrm{d}E/\mathrm{d}s$ and mean free path λ_in can be calculated as follows:

$$\begin{aligned} -\frac{\mathrm{d}E}{\mathrm{d}s} &= \int_0^{E-E_\mathrm{F}} \hbar\omega \,\mathrm{d}\omega \int_{q-}^{q+} \mathrm{d}q \frac{\mathrm{d}^2\lambda_\mathrm{in}^{-1}}{\mathrm{d}q\,\mathrm{d}\omega} \\ &= \int_0^{E-E_\mathrm{F}} \hbar\omega \,\mathrm{d}\omega \int_{q-}^{q+} \mathrm{d}q \frac{\hbar}{\pi a_0 E} \mathrm{Im}\left\{\frac{-1}{\varepsilon(q,\omega)}\right\} \frac{1}{q}. \end{aligned} \tag{2}$$

Here, a_0 is the Bohr radius, E_F is the Fermi energy, q is the transferred momentum, and the integration limits satisfy $\hbar q^\pm = \sqrt{2m}\left(\sqrt{E} \pm \sqrt{E-\hbar\omega}\right)$. Based on the dielectric function theory, the energy loss function $\mathrm{Im}\{-1/\varepsilon(q,\omega)\}$ can be expanded in Lindhard dielectric function $\mathrm{Im}\left\{-1/\varepsilon_\mathrm{L}\left(q,\omega;\omega_\mathrm{p}\right)\right\}$ and the optical energy loss function $\mathrm{Im}\{-1/\varepsilon(\omega)\}$ with the plasmon frequency ω_p as follows:

$$\mathrm{Im}\left\{\frac{-1}{\varepsilon(q,\omega)}\right\} = \int_0^{\infty} \mathrm{d}\omega_{\mathrm{p}} \frac{2}{\pi\omega} \mathrm{Im}\left\{\frac{-1}{\varepsilon(\omega_{\mathrm{p}})}\right\} \mathrm{Im}\left\{\frac{-1}{\varepsilon_{\mathrm{L}}(q,\omega;\omega_{\mathrm{p}})}\right\}, \tag{3}$$

In FPA, the energy loss function can be described as two contributions, *i.e.* the single electron excitation part and plasmon excitation part:

$$\mathrm{Im}\left\{\frac{-1}{\varepsilon(q,\omega)}\right\} = \mathrm{Im}\left\{\frac{-1}{\varepsilon(q,\omega)}\right\}\Big|_{\mathrm{single-e}} + \mathrm{Im}\left\{\frac{-1}{\varepsilon(q,\omega)}\right\}\Big|_{\mathrm{plasmon}}, \tag{4a}$$

$$\mathrm{Im}\left\{\frac{-1}{\varepsilon(q,\omega)}\right\}\Big|_{\mathrm{single-e}} = \int_0^{\infty} \mathrm{d}\omega_{\mathrm{p}} \frac{2}{\pi\omega_{\mathrm{p}}} \mathrm{Im}\left\{\frac{-1}{\varepsilon(\omega_{\mathrm{p}})}\right\} \mathrm{Im}\left\{\frac{-1}{\varepsilon_{\mathrm{L}}(q,\omega;\omega_{\mathrm{p}})}\right\} \Theta\left[q^{+}(\omega;\omega_{\mathrm{p}}) - q\right] \Theta\left[q - q^{-}(\omega;\omega_{\mathrm{p}})\right], \tag{4b}$$

$$\mathrm{Im}\left\{\frac{-1}{\varepsilon(q,\omega)}\right\}\Big|_{\mathrm{plasmon}} = \frac{2}{\pi\omega_0} \mathrm{Im}\left\{\frac{-1}{\varepsilon(\omega_0)}\right\} \frac{\pi}{\left|\partial\varepsilon_{\mathrm{L}}^{1}(q,\omega;\omega_{\mathrm{p}})/\partial\omega_{\mathrm{p}}\right|_{\omega_{\mathrm{p}}=\omega_0}} \Theta\left[q^{-}(\omega;\omega_0) - q\right]. \tag{4c}$$

Here, the Θ is the step function, ω_0 is the solution of $\varepsilon_{\mathrm{L}}^{1}(q,\omega;\omega_0) = 0$. $q^{\pm}$ are the the boundary of the single electron excitation part and the plasmon excitation part, respectively. Here the Hartree atomic unit ($m_{\mathrm{e}} = e = \hbar = 1$) can be used to simplify the calculation, where m_{e} is the electron rest mass, e is the elementary charge, and $\hbar$ is the reduced Planck constant.

During the inelastic scattering, apart from the process between moving electron and extranuclear electron, the electron–phonon process and the electron–polaron process also affect electron transport, especially for low energy electrons. When electron energy is less than the triple material energy gap (about 20 eV), the electron–phonon process is remarkably enhanced. The interaction between free electrons and longitudinal optical phonon (LO mode) for polarization materials can be analyzed by usig Frohlich disturbance theory.[39,40] The electron–phonon process always comes with the generation and absorption of phonon. Based on the Ganachaud and Callier theory, the distribution relationship of longitudinal optical can be ignored in the optical frequency range, and the electron–phonon process can be accurately described as a function of the single frequency ω_{LO}.[41] Based on the Frohlich disturbance theory, the mean free path of electron–phonon $\lambda_{\mathrm{phonon}}^{-1}$ (generating longitudinal optical phonon with energy $\hbar\omega$ induced by the electron with energy E) can be expressed as a function of $\varepsilon(0)$ and $\varepsilon(\infty)$, which are permittivity at low frequency and optical frequency, respectively.

$$\lambda_{\mathrm{phonon}}^{-1} = K(T)\frac{\hbar\omega}{E}\ln\left\{\left[1+(1-\hbar\omega/E)^{1/2}\right]/\left[1-(1-\hbar\omega/E)^{1/2}\right]\right\}, \tag{5}$$

$$K(T) = \frac{1}{a_0}\left|\frac{1+1/\left(\mathrm{e}^{\hbar\omega/kT}-1\right)}{2}\right|\left|\frac{1}{\varepsilon(\infty)} - \frac{1}{\varepsilon(0)}\right|. \tag{6}$$

Here, k is the Boltzmann constant, and T is the absolute Kelvin temperature. The transferred energy from electron to phonon is set to be $W_{\mathrm{ph}} = \hbar\omega = 0.1$ eV. In this simulation, the process of phonon annihilation is ignored because its probability is much less than that of phonon generation. For materials with electric polarization, free electrons with low energy may also be trapped by the polaron. Here, considering that the simulated materials are elementary substances, we ignore the interaction between electron and polaron.

2.2. Energy loss function

The reaction between energetic electron–extranuclear electrons can be described as a dielectric related energy loss function, which is always hardly obtained. Dielectric function $\varepsilon(q,\hbar\omega)$ describes the material response to inner point charge related to momentum transformation q and energy loss $\hbar\omega$. In the limited optical condition $q \to 0$, the dielectric function can be described as $\varepsilon(0,\hbar\omega) = \varepsilon_1 + \mathrm{i}\varepsilon_2$, where ε_1 and ε_2 are the real part and the imaginary part of the dielectric function, respectively. Then the energy loss function can be described as

$$\mathrm{Im}\left[-\frac{1}{\varepsilon(0,\hbar\omega)}\right] = \frac{\varepsilon_2}{\varepsilon_1^2+\varepsilon_2^2} = \frac{2nk}{(n^2+k^2)^2}, \tag{7}$$

where n and k are the refraction index and the extinction coefficient of the material, respectively. Now, the primary method to obtain the energy loss function is based on experiment measurements of n and k. When the electron energy is larger than 72 eV, the n and k data can be calculated by component atoms based on Henke.[42] Acutely, not all n and k data of material are available from the published experimental data in lower energy range <72 eV. This paper uses the first-principles method

to derive the dielectric function ε_1 and ε_2 of graphene on silicon (111) in the lower energy range.

The three-dimensional (3D) lattice structure of graphene on silicon is shown in Fig. 1. The silicon unit cell is set to be in the 2×2 in u–v plane in crystal orientation of (111), and its lattice parameters are (u, v, θ): 7.68017 Å, 7.68017 Å, 120°. The surface graphene unit cell is set to be 3×3 in u–v plane with the lattice parameters are (u, v, θ): 7.379997 Å, 7.379997 Å, 120°. The average lattice parameters of build layers are set to be (u, v, θ): 7.530083 Å, 7. 530083 Å, 120° with the mismatching rate 1.99%. The thickness of the vacuum layer between the layers is set to be larger than 20 Å for building a less interaction vacuum boundary.

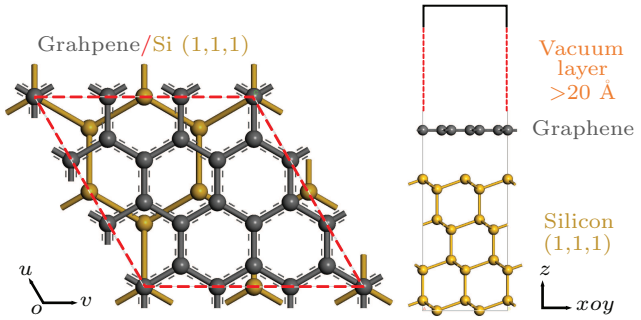


Fig. 1. Vertical view and front view of 3D lattice structure of graphene on silicon.

The energy loss related dielectric function is derived with density functional theory (DFT) based on the first-principles method. In this work, the DFT is calculated via the Cambridge Sequential Total Energy Package (CASTEP, version 2019) software. We first use Broyden–Fletcher–Goldfarb–Shanno (BFGS) for the unit cell structure optimization and select the TS parameters for the van der Waals dispersion correction. Then, we calculate the energy band structure, density of states, and optical properties.[43] The exchange–correlation function in the Kohn–Sham equation is described by LDA (Local Density Approximation).[44,45] The electron wave function is expanded in basis plane wave. The energy cutoff is set to be 400 eV, the convergence precision of the SCF iterative process is set to be 5×10^{-6} eV/atom. The k-points of monolayer graphene and multilayer graphene are set to be $30 \times 30 \times 1$ and $20 \times 20 \times 6$. The actual minimum spacing reaches 0.016 1/Å. The pseudopotential is described with OTFG ultra-soft for calculating electron structure.[46] The imaginary part of the dielectric constant can be described via electron transition probability as follows:

$$\begin{aligned} &\varepsilon_2(\boldsymbol{q} \to 0, \omega) \\ &= \frac{2e^2\pi}{\Omega\varepsilon_0} \sum_{k,v,c} |\langle \psi_{\boldsymbol{k}}^{\mathrm{c}} | \boldsymbol{u} \cdot \boldsymbol{r} | \psi_{\boldsymbol{k}}^{\mathrm{v}} \rangle|^2 \delta(E_k^{\mathrm{c}} - E_k^{\mathrm{v}} - E), \end{aligned} \tag{8}$$

where $\langle \psi_k^{\mathrm{c}} | \boldsymbol{u} \cdot \boldsymbol{r} | \psi_k^{\mathrm{v}} \rangle$ is the position matrix, $\boldsymbol{u}$ is the vector defining the polarization of the incident electric field, E_k^{c} and E_k^{v} are transition energies of conduction band and valence band, and $\boldsymbol{E}$ is the electron energy. The ψ_k^{c} and ψ_k^{v} are the initial wave function and the final wave function, respectively. The matrix elements of the position operator which are required to describe the electronic transitions may normally be written as matrix elements of the momentum operator P, allowing the straightforward calculation in reciprocal space. The corrected form of the matrix elements is

$$\langle \psi_{\boldsymbol{k}}^{\mathrm{c}} | \boldsymbol{r} | \psi_{\boldsymbol{k}}^{\mathrm{v}} \rangle = \frac{1}{\mathrm{i}\omega m} \langle \psi_{\boldsymbol{k}}^{\mathrm{c}} | \boldsymbol{P} | \psi_{\boldsymbol{k}}^{\mathrm{v}} \rangle + \frac{1}{\hbar\omega} \langle \psi_{\boldsymbol{k}}^{\mathrm{c}} (|V_{\mathrm{nl}}|, \boldsymbol{r}) \psi_{\boldsymbol{k}}^{\mathrm{v}} \rangle, \tag{9}$$

where V_{nl} is the position $\boldsymbol{r}$-related nonlocal pseudopotential.

Ultra-soft pseudopotential produces an additional contribution to optical matrix elements that are also included in results. Then, based on the Kramers–Kronig dispersion relation, the real part of the dielectric constant $\varepsilon_1(\omega)$ can also be calculated. The energy loss function with electron energy loss $\hbar\omega$ can be derived from Eq. (7).

When the loss energy is larger than a hundred eV, the inelastic scattering is mainly dominated by the interaction between free electrons and inner shell electrons. The inner shell interaction has an insignificant effect on the exchange–correlation field and is basically independent of each other for atoms. Here, in this simulation, for the situation of inner shell inelastic scattering, we can use the energy loss data by Henke *et al.*[42] And the integrated energy loss function can be related to low energy loss from the outer shell and to high energy loss from the inner shell.

2.3. Monte Carlo simulation

A series of interactions, including the elastic and inelastic scattering after the primary electron irradiation on the material surface, can be described via the Monte Carlo simulation method. By using random numbers for describing the collective behavior of a large number of particles, Monte Carlo simulation is widely used in particle physics fields and engineering discharge simulation.[47,48]

In general, the electron transport process inside the material includes the primary electrons and the generated secondary electrons. As shown in Fig. 2, the simulation process begins with the initial parameters setting, and then calculates each step length via the MFP and a random number. Besides, the classification of scattering types and the judgement of the generation and emission of SEs generation and electrons emission are both determined by random numbers. The generated internal SEs will be treated as the initial electrons of the next step and added to the tracking electrons. Finally, by counting all the emission electrons, we can obtain the information about the secondary electron emission.

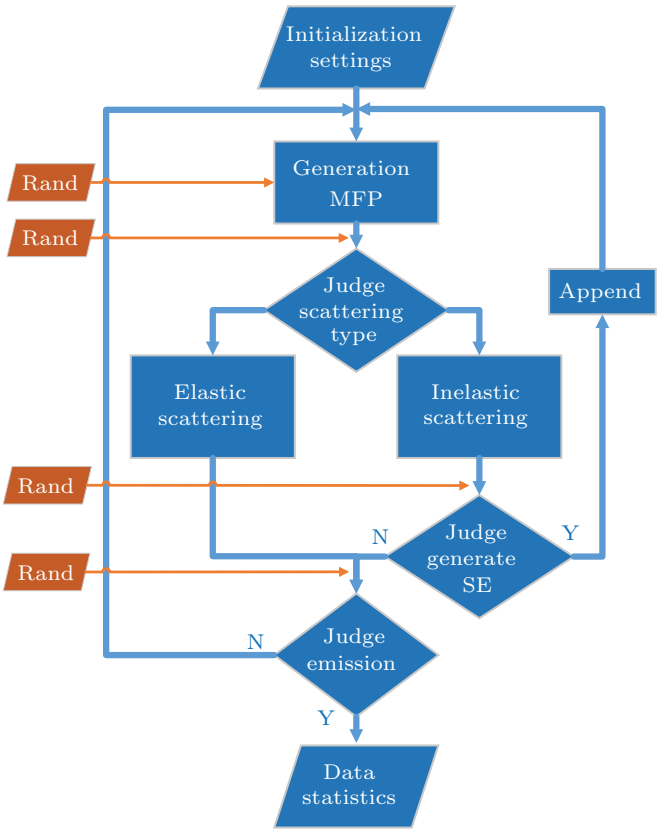


Fig. 2. Flow diagram of secondary electron emission for MC simulation.

Monte Carlo simulation needs to track each electron's movement, and the step between each collision can be described via a random number R_1, $\Delta s = -\lambda \ln R_1$. Here, λ is the total mean free path covering all the mentioned processes,

$$\lambda^{-1} = \lambda_{\rm el}^{-1} + \lambda_{\rm inel}^{-1} + \lambda_{\rm phon}^{-1}. \tag{10}$$

The subscript el, inel, and phon denote the elastic scattering, the electron–electron inelastic scattering, and the electron–phonon process, respectively. The above process that may occur in each collision is judged based on the inverse ratio of each mean free path in total and a random number. When the single collision takes place in the elastic scattering, the scattering angle θ and random number R_2 are related by

$$R_2 = P_{\rm el}(E,\theta) = \frac{1}{\sigma_{\rm el}(E)} \int_0^{\theta} \frac{{\rm d}\sigma_{\rm el}(E,\vartheta)}{{\rm d}\Omega} \sin\vartheta\, {\rm d}\vartheta. \tag{11}$$

When the collision takes place in the form of inelastic scattering, we can obtain the energy loss $\Delta E_{\rm inelastic} = \hbar\omega$ with a random number R_3 as follows:

$$R_3 = \int_0^{\Delta E_{\rm inelastic}} \frac{{\rm d}\sigma}{{\rm d}(\Delta E)} {\rm d}(\Delta E) \Big/ \int_0^{E-E_{\rm F}} \frac{{\rm d}\sigma}{{\rm d}(\Delta E)} {\rm d}(\Delta E). \tag{12}$$

After obtaining the energy loss $\hbar\omega$, we can calculate the scattering angle θ from the formula of random number R_4 which is related to scattering angle θ and momentum conservation $\hbar q$ as follows:

$$R_4 = \int_0^{\theta} \frac{{\rm d}^2\lambda_{\rm in}^{-1}}{{\rm d}\Omega\, {\rm d}\omega} \sin\vartheta'\, {\rm d}\vartheta' \Big/ \int_0^{\pi} \frac{{\rm d}^2\lambda_{\rm in}^{-1}}{{\rm d}\Omega\, {\rm d}\omega} \sin\vartheta'\, {\rm d}\vartheta'. \tag{13}$$

The azimuth angle ϕ satisfies the uniform distribution in a range of 0–π

In FPA, the internal secondary electron generation should also be treated based on the single electron excitation part and the plasmon excitation part.[36] For the plasmon excitation part, the secondary electron is excited from the Fermi sea by loss energy $\hbar\omega$, the excitation probability of initial energy of an excited electron E' is

$$p(E', \hbar\omega) \propto \sqrt{E'(E'+\hbar\omega)}. \tag{14}$$

And for single electron excitation part, the excitation probability of the initial momentum of the excited electron $\boldsymbol{k}_{\rm i}$ is

$$\begin{aligned} & p(|\boldsymbol{k}_{\rm i}| < k_{\rm F}; \boldsymbol{q}, \omega) \\ = & \int {\rm d}\boldsymbol{k}_{\rm i} \Xi \left[\hbar\omega - \frac{\hbar^2}{2m} (2\boldsymbol{k}_{\rm i}\cdot\boldsymbol{q} + q^2) \right] \\ & \times \Theta(k_{\rm F} - |\boldsymbol{k}_{\rm i}|)\, \Theta(|\boldsymbol{k}_{\rm i} + \boldsymbol{q}| - k_{\rm F}). \end{aligned} \tag{15}$$

Here, Ξ is the impulse function.

During inelastic scattering, when the transforming energy is large enough for extranuclear electrons to escape from the nuclear constraint, the loss energy can generate internal free secondary electrons. We still need to follow their trajectories with the same method. For the electron–phonon process, based on Llacer theory,[49] the scattering angle θ can be described with random number R_5 as follows:

$$\cos\theta = \left(\frac{E + E^1}{2\sqrt{EE^1}} \right) (1 - B^{R_5}) + B^{R_5}, \tag{16}$$

$$B = \frac{E + E^1 + 2\sqrt{EE^1}}{E + E^1 - 2\sqrt{EE^1}}. \tag{17}$$

Here, E and E^1 are electron energy before and after the electron–phonon process, respectively.

When the electrons move across the interface between different materials (including the inner interface of graphene–silicon and the surface interface of solid–vacuum), the energy and moving direction will be affected by the interface potential barrier (work function $W_{\rm F}$) $\chi = E_{\rm F} + W_{\rm F}$. Based on the solution of the incident and reflected electron wave functions,[50,51] the penetrating coefficient of electron crossing the interface $T_{\rm interface}$ can be given below:

$$T_{\rm interface} = \begin{cases} 4\left(1 - \dfrac{\chi}{E\cos^2\phi}\right)^{1/2} \Big/ \left[1 + \left(1 - \dfrac{\chi}{E\cos^2\phi}\right)^{1/2}\right]^2, & (\text{if } E\cos^2\phi \geq \chi), \quad (18a) \\ 0, & (\text{if } E\cos^2\phi < \chi). \quad (18b) \end{cases}$$

When the electron energy E and the normal angle ϕ satisfy the inequality: $E\cos^2\phi < \chi$, the penetrating coefficient $T_{\text{interface}} = 0$. As the electron escapes from the surface, it may be treated as the secondary electron emission.

It should be pointed out that although the upper film thickness is comparable to or even less than the electron mean free path (MFP), this MC method may still be used for calculating the SE emission. For monolayer graphene, its thickness is about 0.3 nm, while the electron mean free path ranges from several angstroms to tens of nm, depending on energy. Even so, the Monte Carlo simulation method is still available for describing electron transport within the thin film. In Monte Carlo simulation, each step length is generated by a random number based on the MFP. The actual step length is not a constant of MFP but it is of a probability distribution in a specific range. Hence, the actual step length can be less than film thickness with scattering processes occurring. Owing to the fact that the Monte Carlo simulation relies on statistics of plentiful particle events, the macroscopic result still obeys the physical process.

3. Result and analysis

3.1. Monolayers of GoSi

In the inelastic scattering process, both the scattering angle and internal free secondary electron excitation are determined by the energy loss function. Figure 3 shows the curves of density of states (DOS), dielectric constant and energy loss function calculated with the first-principles method as mentioned before. The curve of DOS of graphene is continuous at fermi energy due to the contribution of p orbital electrons, while for a typical semiconductor, the DOS of silicon presents a forbidden band above the fermi energy as shown in Fig. 3(a).

For the 2D graphene, the different hybridized orbitals show different behaviors in different directions, resulting in the discrepancy between in-plane and out-of-plane energy loss. For the electrons across the graphene layer, the anisotropy of energy loss should also be taken into consideration. In this simulation, we calculate the energy loss function of graphene along the $\boldsymbol{c}$ axis (0, 0, 1) and the $\boldsymbol{a}$ axis (1, 0, 0), while the silicon energy loss function is treated as being isotropic. The composited contribution of the energy loss function can be integrated over all theta directions ($-\pi/2$ to $\pi/2$),

$$\begin{aligned}\text{Im}\left\{\frac{-1}{\varepsilon(\omega)}\right\} = &\int_{-\pi/2}^{\pi/2} \mathrm{d}\theta_{\text{surf}} P_{\text{surf-ang}}(\theta_{\text{surf}}) \\ &\times\left\{\cos^2(\theta_{\text{surf}})\,\text{Im}\left[\frac{-1}{\varepsilon(\omega)}\right]\Bigg|_{\boldsymbol{c}}\right. \\ &\left.+\sin^2(\theta_{\text{surf}})\,\text{Im}\left[\frac{-1}{\varepsilon(\omega)}\right]\Bigg|_{\boldsymbol{a}}\right\}. \quad (19)\end{aligned}$$

Here, θ_{surf} is the surface normal angle, $P_{\text{surf-ang}}(\theta_{\text{surf}})$ is the calculated angle distribution of inner electrons when they reach the surface thin film from sub-material. The energy loss of sub-material silicon is treated as being isotropic. Considering that the energy loss in the plane in each direction is equal, the composited contribution of electron energy loss can be divided into c axis part and a axis part.

For graphene, the real part ε_1 and the imaginary part ε_2 of dielectric constant in the c axis part and the a axis part cross around at the point P (with energy 5.3 eV) and Q (with energy 15.2 eV), respectively, where the energy loss function present two peaks in Fig. 3(b). The peak around 5.3 eV in c axis part results from the plasmon resonance in the π-bond of graphene, while the 15.2 eV peak in a axis part is due to the plasmon resonance in the $\sigma+\pi$-bond of graphene. Those two peaks of the energy loss function also result in the two peaks of inelastic scattering angle distribution. Peaks of imaginary part ε_2 of graphene in the c axis part (at 11.2 eV and 14.5 eV) and in the a axis part (at 0.79 eV, 4.0 eV, and 13.8 eV) correspond to different electron energy level transitions in Fig. 3(a).

Comparing the dielectric constants in Fig. 3(b) with the PDOS in Fig. 3(a), we can find that peaks at 0.79 eV, 4.0 eV, and 13.8 eV of the imaginary part ε_2 of a axis part in Fig. 3(b) may primarily result from the electrons transiting from valence band p orbital to conduction band p orbital in Fig. 3(a). And, peaks at 11.2 eV and 14.5 eV of the imaginary part ε_2 of c axis part may primarily result from the electrons transiting from valence band p orbital to conduction band s orbital. For silicon, the real part ε_1 and imaginary part ε_2 of the dielectric constant cross around the loss energy 17.4 eV, corresponding to a single peak of the energy loss function. The prominent peak of the imaginary part ε_2 of silicon is around 7.0 eV, also denoting the dominated electron energy level transitions. After obtaining energy loss functions in a axis part and c axis part, we can calculate the composited contribution of the energy loss function based on Eq. (19) in Fig. 3(c). On the whole, the single peak of silicon energy loss function presents much higher intensity than π and $\sigma+\pi$ peak of graphene.

Figures 4(a) and 4(b) show the energy loss function of Si and monolayer graphene by using the mentioned full Penn algorithm. The energy loss function is affected by energy loss, $\hbar\omega$, and momentum transfer $\hbar q$. For Si in Fig. 4(a), the energy loss function forms the sharp Bethe ridge along with both energy loss and momentum transfer directions, while the Bethe ridge appears multimodal and gentler. The entire $\hbar\omega$–$\hbar q$ coordinate region includes the single electron excitation part and plasmon excitation part. When the momentum transfer equals 0, the energy loss function degrades into the optical limiting energy-loss function.

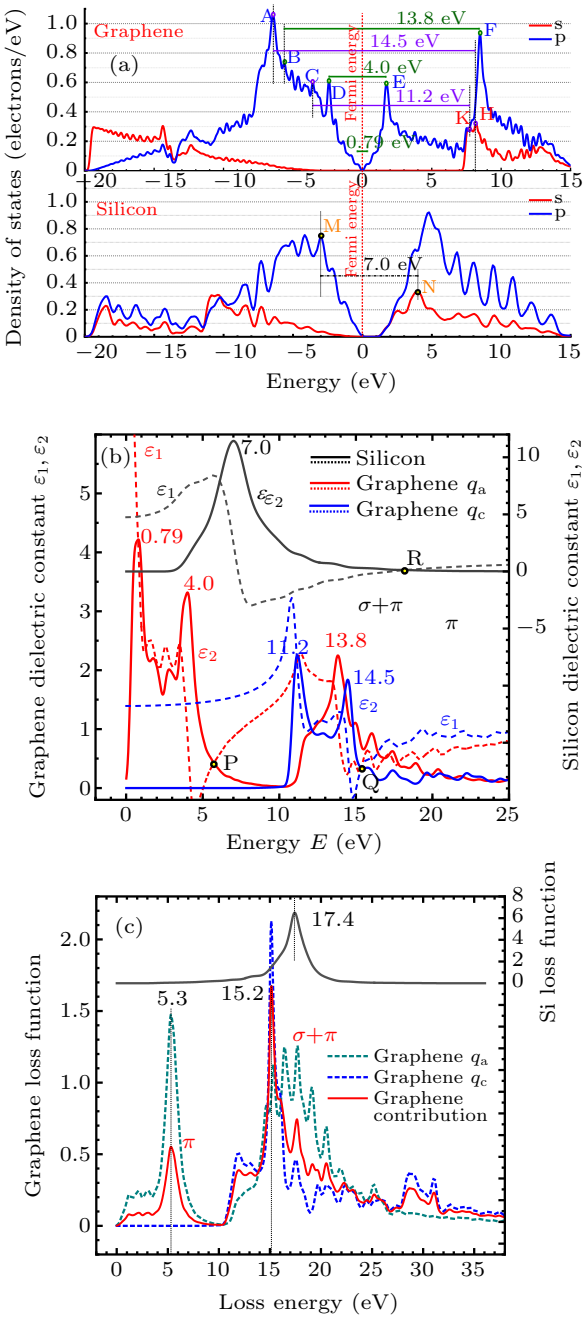


Fig. 3. Curves of (a) graphene density of states and (b) graphene dielectric constants (ε_1 and ε_2) *versus* energy, and (c) curves of graphene loss function *versus* loss energy.

In the process of elastic scattering, only the motion direction of the energetic electron changes under the force between the electron and atomic nucleus, while both direction and energy of electron change during inelastic scattering. Figures 5(a) and 5(b) are electron scattering angle distributions at different electron energy of silicon and graphene. When the electron energy is low, such as 20 eV, the scattering angle presents two peaks (at $\sim 23^\circ$ and $\sim 96^\circ$ for silicon, at $\sim 34^\circ$ and $\sim 148^\circ$ for graphene). The secondary peak recovers and vanishes gradually with electron energy increasing, while the prominent peak increases and becomes sharp towards a slight scattering angle. It shows that the influence of elastic scattering on motion direction is less for high energy electrons.

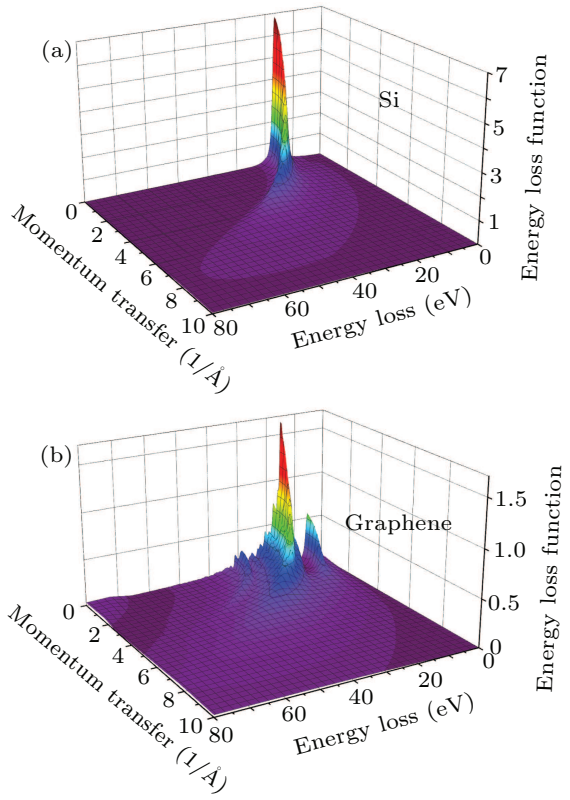


Fig. 4. Energy loss function of (a) Si and (b) monolayer graphene via full Penn algorithm.

Figure 5(c) gives the tendencies of average scattering angle varying with electron energy of silicon and graphene. In general, the elastic scattering angle and the inelastic scattering angle decrease with electron energy: the inelastic scattering angle of graphene is significantly less than that of silicon, while the elastic scattering angle of graphene is less than that of silicon when the electron energy is larger than 150 eV. We need to evaluate the probability of each inner energetic electron occurring in elastic and inelastic scattering P_{Elastic} and $P_{\text{Inelastic}}$, which are defined as $P_{\text{Elastic}} = \lambda_{\text{el}}^{-1} / \left(\lambda_{\text{el}}^{-1} + \lambda_{\text{inel}}^{-1}\right) = 1 - P_{\text{Inelastic}}$. Figure 5(d) shows the variations of elastic and inelastic scattering probability with electron energy for silicon and graphene. We can find that both for silicon and for graphene, the elastic scattering probability is larger than inelastic one when energy is less than 10^3 eV. Although the elastic scattering probability of silicon presents a first-decrease-and-then-increase tendency in which its value is kept larger than 0.64, and the elastic scattering probability of graphene decreases close to the inelastic scattering probability when the electron energy reaches 10^3 eV.

To verify the secondary electron emission by using the above-mentioned method, we compare the calculated secondary electron yield with experiment results from recent reports and our measurements. Figures 6(a) and 6(b) show our secondary electron measurement system and testing schematic diagram, respectively. The system consists of the pre-

processing chamber (on the left) and the analysis chamber (on the right). The sample placed on the holder is covered with a three-layer shield grid to collect the emitted electrons more effectively in the analysis chamber. The background vacuum degree of the analysis chamber is maintained via a 3-level vacuum pump within 10^{-8} Pa. The pulsed E-beam gun works in a range from 30 eV to 3 keV, with the emission current ranging from 50 pA to 50 μA. To avoid strongly charging state on the dielectric surface, the system sets a neutralization low energy E-beam gun *in situ* and works in a range of 2 eV–100 eV. A positive +38 V bias voltage is added to the collection grid, and the collected current is obtained via a picoammeters Keithley 6487E. The secondary electron yield can be measured via the E-beam gun current J_{PE} and collected current J_C as SEY $= J_C/J_{PE}$, where the SEY stands for the secondary electron yield.

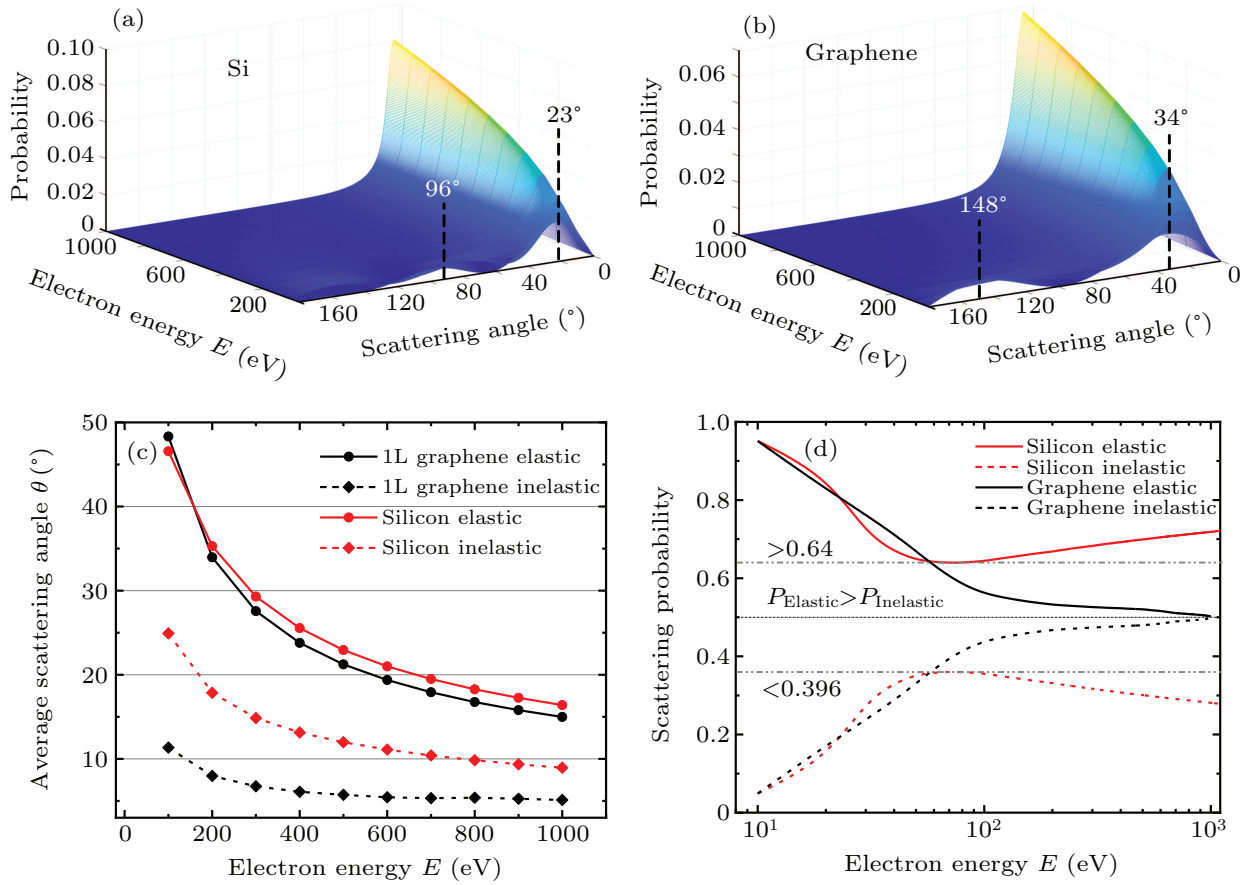


Fig. 5. Elastic scattering probability and angle of (a) silicon and (b) graphene, (c) variations of average scattering angle with electron energy of elastic and inelastic scattering in graphene and silicon, (d) variations of elastic and inelastic scattering probability with electron energy of silicon and graphene.

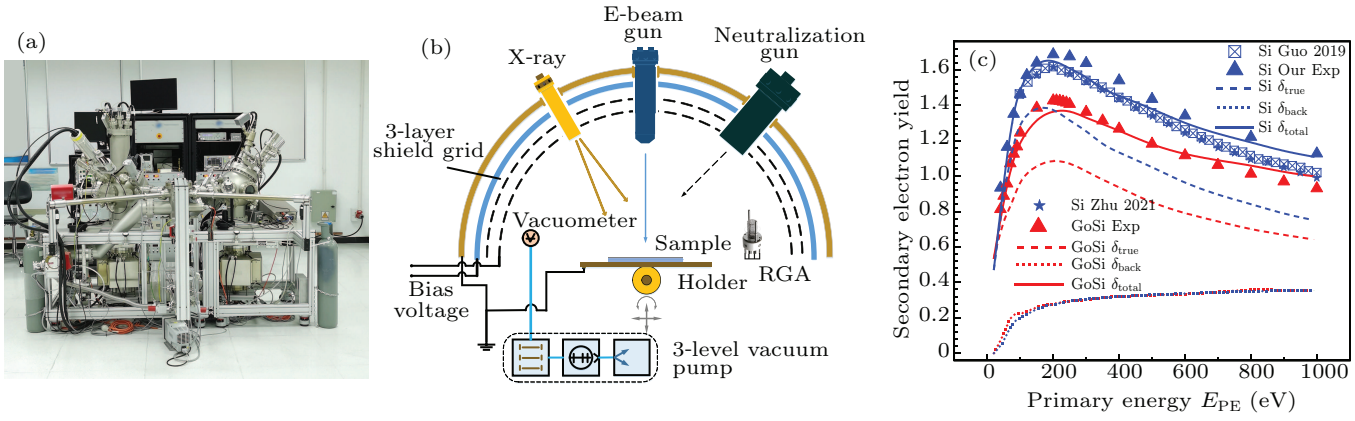


Fig. 6. (a) Diagram of secondary electron generation, (b) measurement system, and (c) comparison among secondary electron yields.

In measuring the secondary electrons emitted from a dielectric material, factors of surface microstructure morphology, adsorption states, and charge accumulation will significantly affect the measured results, which results in experiment data varying in a significant range. Here, we compare this simulation results of secondary electron yield with the counterparts for recent references and our experiment measurements as shown in Fig. 6(c).[52,53] The deviations between simulation results and different experiments are existent, especially for monolayer graphene on silicon. Apart from measurement uncertainty, interface contamination and defect may both increase the deviation.

3.2. Few layers of GoSi

To further investigate the secondary electron emission characteristics in graphene layers, we also investigate the electron interaction with one to four layers of graphene on silicon. Since the potential field in multilayer graphene may be changed due to the exchange–correlation effect across the layers. We calculate the surface work function and the energy loss function in one to four layers of graphene on silicon. Here, in order to avoid the fringe effect in periodic boundary as much as possible, the sub-based material is set to be of four layers, and the vacuum layer is set to be 20-Å thick. The surface work functions and the average potential profiles of one to four layer GoSi are shown in Fig. 7. Under the van der Waals force between silicon and graphene, for the 1 layer of GoSi as shown in Fig. 7(a), the maximum average potential of interface rises to 5.43 eV in comparison with the potential in periodic structural gap of silicon. With the number of graphene layers increasing, the van der Waals force tends to be balanced, and this average potential difference decreases to 3.77 eV, 3.16 eV, and 3.06 eV for 2–4 layers of GoSi respectively. The values of surface work function W_f of 1–4 layers of GoSi are determined to be 4.22 eV, 4.37 eV, 4.48 eV, and 4.41 eV, respectively, by the difference between Fermi energy and vacuum energy, under the combined effect of graphene potential and interface potential. Compared with Si (111) surface, as shown in Fig. 7(b), the work function W_f of the monolayer of GoSi decreases from 4.43 eV to 4.22 eV. With layer number increasing, work function W_f of GoSi increases to that of the graphite. The dotted line in Fig. 7(b) shows the ultimate value of the work function for a giant layer number graphene about 4.43 eV, which is close to the value reported previously.[54]

In the microscopic perspective, the geometrical parameter and the electron density distribution may vary for multilayer graphene on silicon as shown in Fig. 8. The GoSi system is optimized and its total energy reaches a minimum value in geometry optimization. To obtain the minimum energy of system, in the geometry optimization process, we relax silicon atoms in surface four layers and all of coating graphene C atoms. Since the strength of graphene CC bond is much stronger than that of the Si–Si bond, the C atom in a layer graphene presents a slight displacement. Owing to a weak Van der Waals interface force for the monolayer graphene on silicon, the minimum interface distance reaches 2.89 Å, which is larger than the counterpart in other multilayer graphene situations. However, under the imbalanced Van der Waals forces from two sides for a fewer-layer GoSi (1–2 layers), the electron density difference of top silicon atoms (as the denoted district in Fig. 5) presents a noticeable positive expansion. For the situation of more layers GoSi (3–4 layers), Van der Waals forces from two sides come to be more balanced, and the electron density difference deviation gradually vanishes. It is also the reason that the difference of interlayer peak potential decreases with graphene layers increasing as shown in Fig. 8(a). And the interlayer distance of graphene layers keeps a constant of 3.30 Å, while the interval of the upper graphene layer enlarges slightly, from 3.31 Å to 3.33 Å of 2 layers to 4 layers. Finally, under the combined effects of both the deviation of interface electron density difference and the variation of upper layer interval, the work function value of GoSi changes from 4.22 eV of 1 layer to that of graphite situations as the number of graphene layers increases. The apparent positive deviation of electron density difference leads the work function of 1 layer of GoSi to be less than that of non-coated Si (111) and graphite situation.

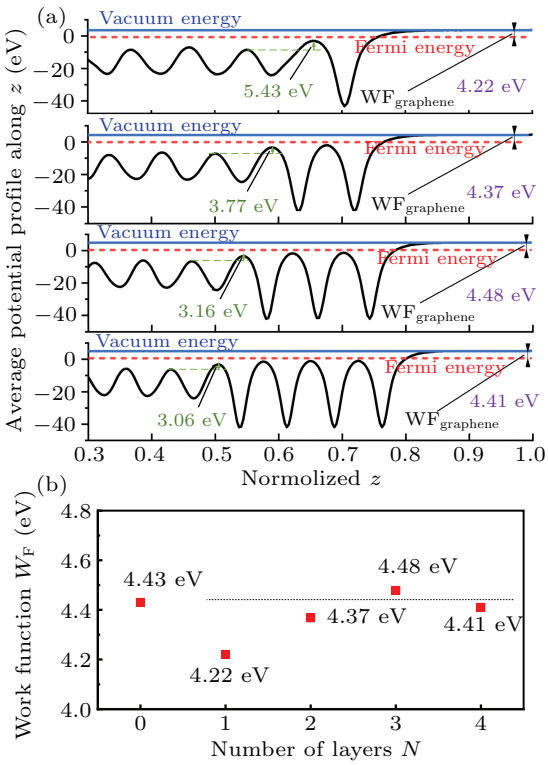


Fig. 7. (a) Average potential profiles against normolized z, and (b) work function *versus* layer number.

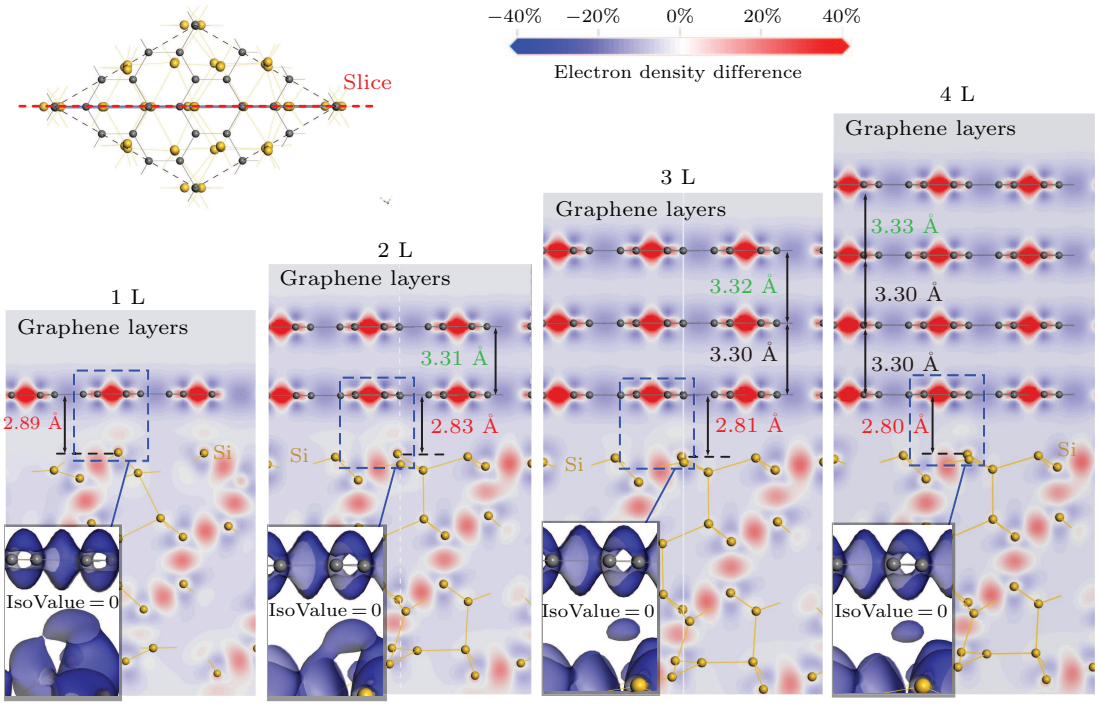


Fig. 8. Electron density differences of multilayer (1–4 layers) graphene on silicon.

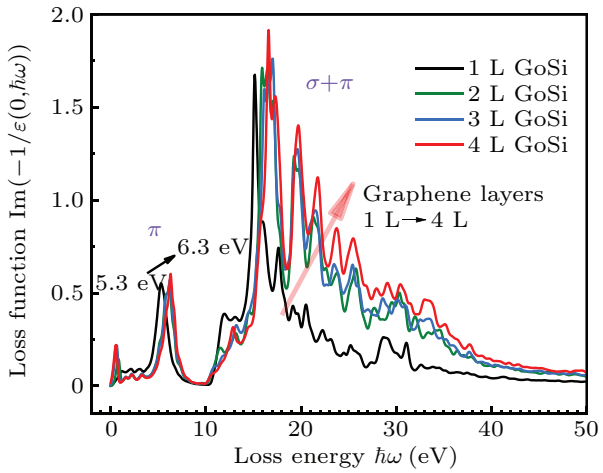


Fig. 9. Energy loss functions of one to four layer graphene.

Figure 9 shows the electron energy loss function inside one to four layers of graphene. We can find that with the increase of layer number, the π peak and the $\sigma+\pi$ peak present the tendency of moving toward higher energy and enhancing. Compared with the scenario in Ref. [55], the tendencies of the right-movement of π peak and the enhancement of $\sigma+\pi$ peak basically agree with the simulation results. The value difference may result from the charge migration and structure variation due to the sub silicon interaction. The π peak energy moves from 5.3 eV of 1 layer to 6.3 eV of 4 layers, and the $\sigma+\pi$ peak energy moves from 15.2 eV of 1 layer to 16.6 eV of 4 layers. It indicates that the coupling effect of multilayer increases the out-of-plane π peak energy and the in-plane $\sigma+\pi$ peak energy, and also enhances their intensities of energy loss. Because the interaction from sub-layer material on the surface decreases with distance increasing, the effect of layer numbers on the surface work function decreases rapidly. Based on previous researaches,[56,57] the work function reaches its stable value after layer number becomes larger than 4. For the body properties, the range affected by layer number is larger. For example, for the energy loss function, it is found that the EELS of 5-layer graphene is obviously different from that of graphite until the layer number is larger than 10.[55]

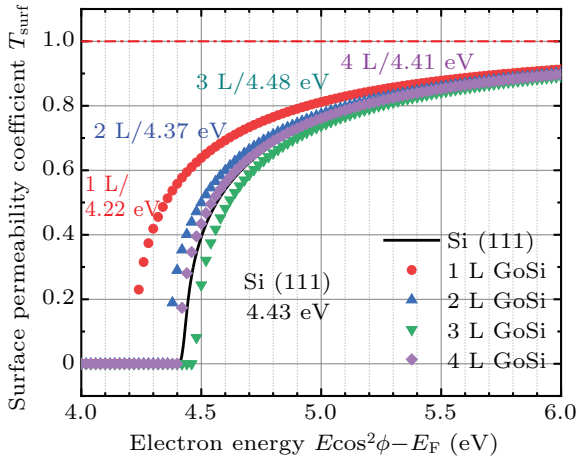


Fig. 10. Variations of electron permeability coefficient T_{surf} with electron energy for different number layers GoSi.

Figure 10 shows the penetration coefficient T_{surf} when electrons pass through the solid-vacuum's surface potential barrier, obtained from Eq. (18a). We can find that only the free electrons whose energy is larger than the surface work function W_F may pass through the surface to form an outgoing secondary electron. Even so, part of electrons with energy

larger than W_F may still reflect back. For instance, the probability of 5 eV electrons reflecting back from 1 layer GoSi surface still reaches 19%. A low surface work function, such as 1 layer GoSi, still comes with a greater electron emission than Si (111) surface work function. Here in Fig. 10, the electrons are assumed to pass through the surface vertically. For other directions, the electron energy in the x-axis direction should still be multiplied by $\cos^2\phi$.

After passing through the surface interface, the secondary electron emission present various characteristics in different layers of GoSi as shown in Fig. 11. Comparing with the original silicon (111) surface, the secondary electron yields from 0–4 layers of graphene on silicon decrease from 1.65 to 1.11–1.12. It is mainly because, on the one hand, as denoted in Fig. 10, the surface coating graphenechanges the electron emission potential barrier due to the fact that a lot of surface-around low energy electrons still keep on escaping. Owing to a lower work function of 1-layer GoSi, the surface potential barrier of fewer layers (1–2 layers) graphene coatings cannot contribute to the suppression of secondary electron emission. Conversely, the energetic freemoving electrons can easily go to the inner with an apparently less elastic scattering angle in graphene. Electrons inside the graphene layers are accompanied with a more extensive in-plan energy loss with a prominent peak of 15.2 eV, while the energy loss peak of silicon is around 17.4 eV. In addition, the smaller scattering cross section of graphene also results in a lower collision probability, which means that the electrons tend to dissipate more deeply inside the graphene than inside silicon. So, under the two inverse factors of surface potential barrier and internal scattering process, the total emission secondary electron yield of 1-layer GoSi (the maximum secondary electron yield $\delta_{max} = 1.38$) is obviously lower than that in the silicon (111) situation ($\delta_{max} = 1.65$) as shown in Fig. 11. But, with the increase of graphene layer number, the recede of interface electron density difference deviation promotes the recovery of surface W_F of GoSi, and also enlarges the range of electron scattering process in graphene. Those two factors both inhibit the secondary electron emission as shown in Fig. 11(a). The value of δ_{max} decreases from 1.38 to 1.12, and the primary energy of maximum secondary electron yield E_{max} also recedes from 229 eV to 165 eV for 1–4-layers GoSi. In Fig. 11(b), we find that the δ_{max} acts as an exponential function of the graphene layers number N_{layer}, $\delta_{max}(N_{layer}) = a\cdot\exp((1-N_{layer})/b) + \delta_{lim}$. Here, a is the parameter related to coating material, which is fitted as 0.28, and b is the parameter related to single-layer thickness, which is fitted as 1.34. The δ_{max} is indicated as the limit value of the maximum secondary electron yield increasing with layer number increasing, and it is 1.06 in this case.

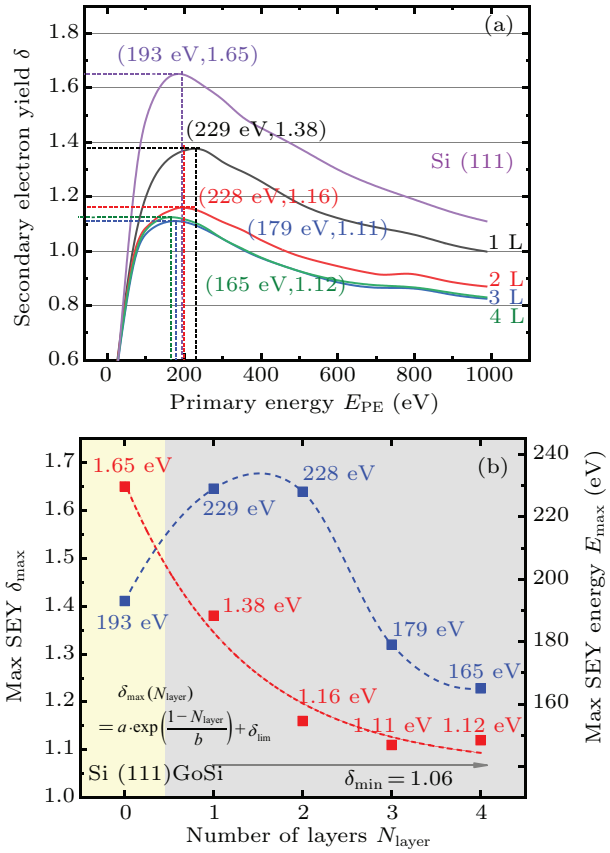


Fig. 11. (a) Curves of secondary electron yield *versus* primary energy, and curves of maximum SEY and the Max SEY energy *versus* number of layers from 0- to 4-layer graphene on silicon (111) surface.

Under the two effects, *i.e.* the surface work function barrier and the inner scattering intrinsic properties, the graphene layer can effectively reduce the emitted secondary electrons. The dominant effect causing such a reduction in the emission process remains controversial. Researchers always use different factors to explain phenomena, thus drawing conflicting conclusions sometimes. In order to more directly demonstrate which of those two factors (the surface work function and inner intrinsic properties) makes a dominant contribution to the secondary electron yield, we compare the situation with the case of four GoSi samples with different layers, and the results are shown in Fig. 12. The contribution of work function to GoSi SEY suppression is defined as

$$C_{WF} = 1 - \frac{\Delta\delta_{max}|_{WF_{GoSi}=WF_{Si}}}{\Delta\delta_{max}}, \tag{20}$$

where $\Delta\delta_{max}$ is defined as the reduction value by comparing GoSi with Si (111), *i.e.* $\Delta\delta_{max} = \delta_{max}|_{GoSi} - \delta_{max}|_{Si\ (111)}$. The subscript $WF_{GoSi} = WF_{Si}$ in $\Delta\delta_{max}|_{WF_{GoSi}=WF_{Si}}$ denotes that the GoSi work function is supposed to be the same as Si (111). For the situations of 1–2-layers GoSi, the values of $\Delta\delta_{max}|_{WF_{GoSi}=WF_{Si}}$ (0.32 and 0.50) are larger than true values of $\Delta\delta_{max}$ (0.28 and 0.493), thus, the values of C_{WF} are negative, *i.e.* −13.2% and −1.4% for SEY suppression. With the increase of graphene layer number (3–4 layers GoSi), al-

though the $\Delta\delta_{max}|_{WF_{GoSi}=WF_{Si}}$ is larger than $\Delta\delta_{max}$, the values of C_{WF} are merely 1.0% and −0.3% for the SEY suppression. It suggests that the surface potential barrier of fewer graphene layer GoSi (1–2 layers) may inversely promote the secondary electron emission, which hardly contribute to SEY suppression even for more layers of GoSi (3–4 layers). The inhibition effect of graphene on SEY is mainly by inducing the deeper electrons in the scattering process. Besides, what should be noted is that for other base materials, various Van der Waals interface forces may result in the effects on work function to varying degrees or even leads to the converse effects on work function.

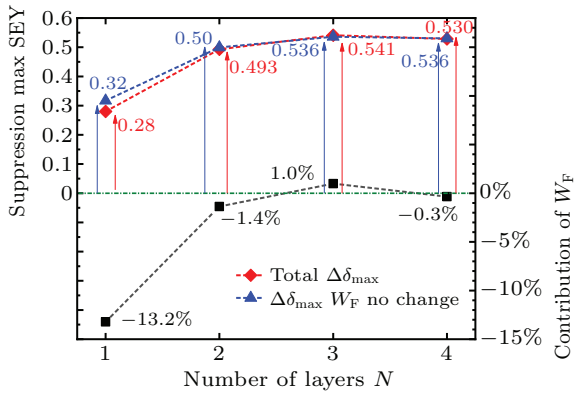


Fig. 12. Contributions of work function to SEY suppression in different layer numbers of GoSi.

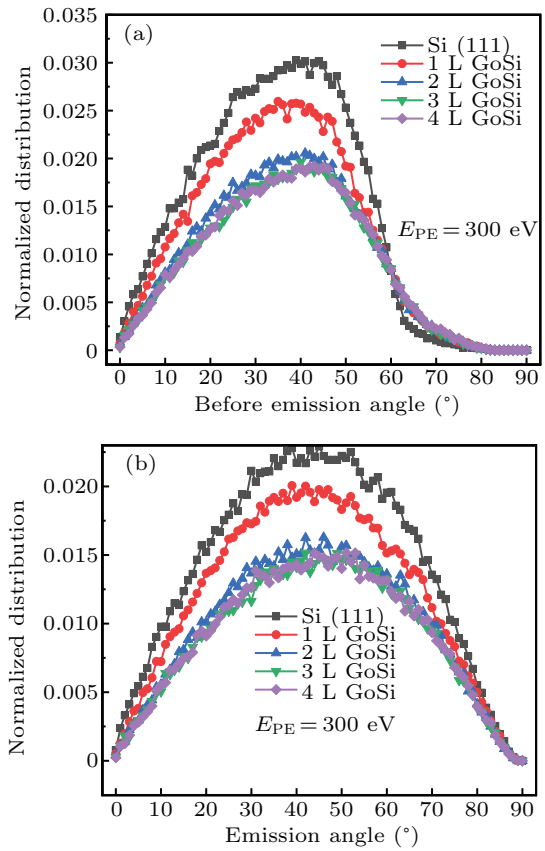


Fig. 13. Angle distributions from different layer number GoSi (a) before and (b) after emission.

When the emission electrons pass through the surface, the emission angle may also be changed by the potential barrier. The energy and angle of the electron entering and exiting obey the refraction law $\sqrt{E_{in}}\sin\alpha = \sqrt{E_{out}}\sin\beta$. Figures 13(a) and 13(b) show the normalized angle distribution before and after emission from the surface. Based on the refraction law, considering the critical angle, the angle of electron entering into the surface potential barrier is almost under 70° for the situation of primary energy 300 eV. The angle distribution before emission is more centralized for Si (111) surface than for GoSi, and the graphene layer results in angle distribution that becomes flatter as the layer number increases. Hence, the angle distribution after emission presents a sine distribution and also becomes flatter from Si (111) and 1-layer to 4-layer GoSi.

Since moving electrons exhibit various behaviors when residing inside the materials with different intrinsic properties or passing through the interface, the distribution of deposited electrons also presents various characteristics inside different layer-number GoSi, which can also explain the corresponding various SEYs from the inside viewpoint. Figure 14(a) shows the true SE emission proportions and internal deposited SE distributions in depth of 2-layer GoSi under 100 eV, 300 eV, 500 eV, and 800 eV electron-beam irradiation. We can find that most of the true SE emissions exit from 20-Å depth. Hence, the multiplication of internally deposited electron distribution and emission electron proportion in this region correlate with the SEY. As shown in Fig. 14(a), when the primary energy is 300 eV, the emission electron proportion becomes flatter in depth. It is mainly because the situation with primary energy 300 eV comes with a larger inelastic scattering section around the surface than the situation with higher 800 eV. Meanwhile, it can generate more energy loss than the situation with the lower 100 eV as indicated by the dash lines in Fig. 14(a). It results in the SEY for 300 eV being larger than for 100 eV and 800 eV. In addition, comparing with graphene layers and sub-silicon, the internal electron distribution appears to have a remarkable sharp rise, resulting from the difference in scattering process and the defect and potential barrier around the interface.

For different layer-number GoSi as shown in Fig. 14(b) in primary energy E_{PE} = 300 eV, as the number of layers increases, the solid red line (4 layers) decreases with depth faster than the blue and black lines (1–2 layers), which means that more SEs are emitted from the surface region of the bigger-layer-number graphene. Meanwhile, for the graphene layer with a smaller elastic scattering cross section, deposited SEs in graphene region decrease with layer number increasing from 1 to 4, indicating the excited SE quality in graphene region decreases. Consequently, under the combining effects of those

two distributions (the emission SE position and the excited SE position), internal SEs that can reach the sample surface become less for a thicker graphene-coated GoSi. Moreover, a larger surface work function further results in less SE emission.

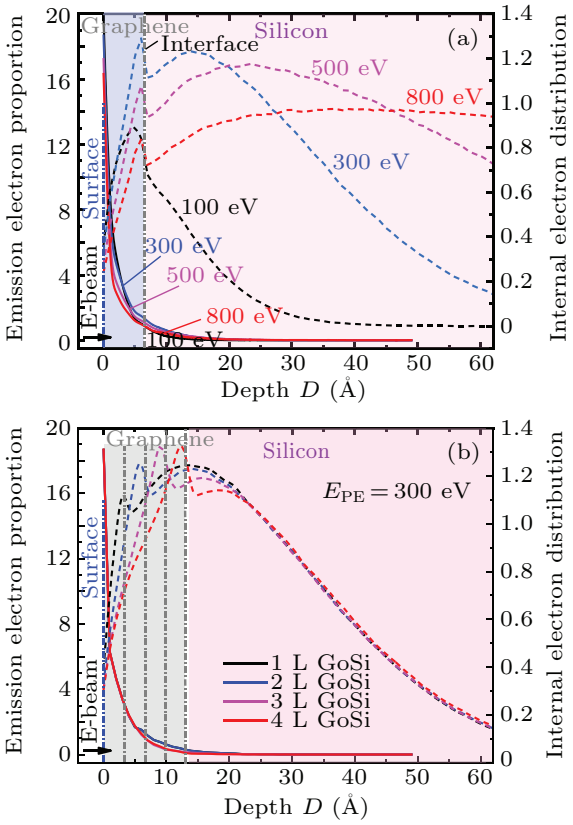


Fig. 14. Internal electrons distributions of graphene on silicon for (a) under different incident energies and (b) different layer numbers of GoSi.

In addition, when calculating interface with DFT, in order to reduce the cell size, a mismatch is alway created due to the uniformity of the material lattice constants on both sides of the interface, which may have an influence on the absolute value of material properties. Nevertheless, in this study, the intrinsic mechanisms and characteristics are still kept consistently since the cases considered are all under the same mismatch parameters. Here, we only investigate the situation of graphene on silicon (111) crystal face. As for other crystal faces, such as (110) or (100), the method proposed in this study is still applicable to the calculating of the SEY. It should be noted that the interface matching requirement may make the calculation much longer due to a larger size unit cell.

Here, we choose a large atom-density crystal face at the interface Si (111) as a typical semiconductor substrate for coating graphene layers in this research. Although owing to the different surface atom densities and the interface matching state, the work function, and interface potential could be different from those of other directional crystal surface, this method of calculating SE emission is also appropriate to other situations. In practice, the substrate silicon wafer is easily oxidized to form a dangling bond with the O atom. Hence, for forming a pure silicon surface, the silicon substrate should first experience the process of outgassing at a temperature higher than 600 °C in an UHV environment less than 10^{-10} mbar (1 bar = 10^5 Pa) UHV for 24 h. Then, after repeatedly flash-heating in 5×10^{-9}-mbar UHV to over 1200 °C, the silicon substrate could present the equilibrium structure of Si (111) without dangling bond. Actually, the dangling bond will change the surface binding energy and the interface potential. A thicker interface oxide layer can also be treated as an extra layer to influence the secondary electron emission bychanging the inner electron collision process. Those related characteristics will be investigated in further researches.

4. Conclusions

In this work, we investigated the electron interaction and SE emission of few layer graphene coated on silicon with a first-principles method based on Monte Carlo numerical simulation. The electron interaction inside the GoSi is calculated with considering elastic scattering via the Mott model, and inelastic scattering via the Full Penn Algorithm of the dielectric function model. The energy loss function is calculated via the first-principles method based on the energy level transition theory. From this study some conclusions can be obtained below. (i) With reverse effects of the surface potential barrier and internal scattering process on SE emission suppression, monolayer graphene can still reduce the maximum SEY to 1.38 from the original silicon 1.65. (ii) When the layer number of graphene increases from 1 to 4, because of the coupling effect of multilayers, both the out-of-plane π energy loss peak and the in-plane $\sigma + \pi$ energy loss peak shift toward higher energy. The maximum SEY further decreases from 1.38 to 1.12 of 1 to 4 layers, behaves as a negative exponential function of graphene layer number. (iii) Owing to the positive deviation of electron density difference at the graphene–silicon interface, the surface work function of monolayer GoSi is pulled down to 4.22 eV from Si (111) 4.43 eV. The work function contribution of monolayer GoSi to the SEY suppression reversely reaches −13.2%, and even for 3-layer GoSi, the work function contribution is just positive 1.0%. The dominant factor of the SEY inhibition for GoSi is the mechanism by inducing electrons more deeply in the scattering process. This research can contribute to the understanding of the microscopic mechanism of electron emission from the coated graphene and has reference significance in suppressing the secondary electron multiplication effect in many engineering fields.

Acknowledgements

Project supported by the National Natural Science Foundation of China (Grant Nos. 61901360 and 12175176), the Natural Science Foundation of Shaanxi Province, China (Grant No. 2020JQ-644), and the Scientific Research Projects of the Shaanxi Education Department, China (Grant No. 20JK0808).

References

[1] Chang C, Liu G Z, Tang C X, Chen C H, Shao H and Huang W H 2010 *Appl. Phys. Lett.* **96** 111502
[2] Rasch J, Anderson D and Semenov V E 2013 *J. Phys. D: Appl. Phys.* **46** 505201
[3] Rozario N, Lenzing H F, Reardon K F, Zarro M S and Baran C G 1994 *IEEE Trans. Microwave Theory Tech.* **42** 558
[4] Nagesh S K, Revannasiddiah D and Shastry S V K 2005 *Pramana* **64** 95
[5] Arregui I, Teberio F, Arnedo I, Lujambio A, Chudzik M, Benito D, Lopetegi T, Jost R, Görtz F, Gil J, Vicente C, Gimeno B, Boria V E, Raboso D and Laso M A G 2013 *IEEE Trans. Microwave Theory Tech.* **61** 4376
[6] Graves T P, Hubble A A and Partridge P T 2016 *IEEE International Conference on Plasma Science (ICOPS)*, June 19–23, 2016, Banff, AB, Canada, p. 1
[7] Shen F, Wang X, Cui W Z and Ran L 2020 *IEEE Trans. Plasma Sci.* **48** 433
[8] Kudsia C, Cameron R and Tang W 1992 *IEEE Trans. Microwave Theory Tech.* **40** 1133
[9] Tang W and Kudsia C M 1990 *IEEE Conference on Military Communications*, September 30–October 3, 1990, Monterey, CA, USA, pp. 181–187
[10] Hubble A A, Feldman M S, Partridge P T and Spektor R 2019 *Phys. Plasmas* **26** 053502
[11] Wang H, Bai X, Liu L, Liu D and Meng L 2020 *Plasma Sources Sci. Technol.* **29** 125012
[12] Nistor V, Gonzalez L A, Aguilera L, Montero I, Galan L, Wochner U and Raboso D 2014 *Appl. Surf. Sci.* **315** 445
[13] Zhang X, Xiao Y T and Gimeno B 2020 *IEEE Trans. Electron Dev.* **67** 5723
[14] Liu L, Feng G B, Chen B D, Wang N and Cui W Z 2021 *AIP Adv.* **11** 025332
[15] Montero I, Aguilera L, Davila M E, Nistor V C, Gonzalez L A, Galan L, Raboso D and Ferritto R 2014 *Appl. Surf. Sci.* **291** 74
[16] Wang J, Wang Y, Xu Y H, Zhang Y X, Zhang B and Wei W 2016 *Chin. Phys. C* **40** 117003
[17] Riccardi P, Cupolillo A, Pisarra M, Sindona A and Caputi L S 2012 *Appl. Phys. Lett.* **101** 183102
[18] Cao M, Zhang X S, Liu W H, Wang H G and Li Y D 2017 *Diamond Relat. Mater.* **73** 199
[19] Wang X J, Wang D W and Li Y D 2018 *Journal of Mechanical Engineering* **54** 115
[20] Ye M, He Y N, Hu S G, Wang R, Hu T C, Yang J and Cui W Z 2013 *J. Appl. Phys.* **113** 074904
[21] Hu X C, Zhang X W, Zhang R and Gu W P 2020 *Results Phys.* **19** 103475
[22] Vaughan J R M 1989 *IEEE Trans. Electron Dev.* **36** 1963
[23] Furman M A and Pivi M T F 2013 *Phys. Rev. Spec. Top-Ac* **16** 069901
[24] Li Y D, Yang W J, Zhang N, Cui W Z and Liu C L 2013 *Acta Phys. Sin.* **62** 077901 (in Chinese)
[25] Ding Z J and Shimizu R 1996 *Scanning* **18** 92
[26] Feng G B, Liu L, Cui W Z and Wang F 2020 *Chin. Phys. B* **29** 048703
[27] Nguyen H K, Mankowski J, Dickens J C, Neuber A A and Joshi R P 2017 *Phys. Plasmas* **24** 124501
[28] Mao S, Li Y, Zeng R and Ding Z J 2009 *J. Appl. Phys.* **104** 114907
[29] Penn D R 1987 *Phys. Rev. B* **35** 482
[30] Khan M, Xu J N, Chen N and Cao W B 2012 *J. Alloys Compd.* **513** 539
[31] Berahman M, Asad M, Sanaee M and Sheikhi M H 2015 *Opt. Quantum Electron.* **47** 3289
[32] Derkaoui Z, Kebbab Z, Miloua R and Benramdane N 2009 *Solid State Commun.* **149** 1231
[33] Ueda Y, Suzuki Y and Watanabe K 2018 *Appl. Phys. Express* **11** 105101
[34] Ewski Z, Maccallum D, Romig A and Joy D C 1990 *J. Appl. Phys.* **68** 3066
[35] Yan R Q, Cao M and Li Y D 2020 *Materials* **15** 3315
[36] Mao S F, Li Y G, Zeng R G and Ding Z J 2008 *J. Appl. Phys.* **104** 114907
[37] Shinotsuka H, Tanuma S, Powell C J and Penn D R 2012 *Nucl. Instrum. Methods Phys. Res., Sect. B* **270** 75
[38] Shinotsuka H, Tanuma S, Powell C J and Penn D R 2015 *Surf. Interface Anal.* **47** 871
[39] Ashley J C 1988 *J. Electron Spectrosc. Relat. Phenom.* **46** 199
[40] Fröhlich H and Taylor A W B 1964 *Proc. Phys. Soc.* **83** 739
[41] Fröhlich H and Mitra T K 1968 *J. Phys. C: Solid State Phys.* **1** 548
[42] Henke B L, Gullikson E M and Davis J C 1993 *At. Data Nucl. Data Tables* **54** 181
[43] Head J D and Zerner M C 1985 *Chem. Phys. Lett.* **122** 264
[44] Perdew J P, Burke K and Ernzerhof M 1996 *Phys. Rev. Lett.* **77** 3865
[45] Perdew J P, Ruzsinszky A and Csonka G I 2008 *Phys. Rev. Lett.* **100** 136406
[46] Dong W, Kresse G, Furthmüller J and Hafner 1996 *Phys. Rev. B* **54** 2157
[47] Feng G B, Cao M, Yan L P and Zhang H B 2013 *Micron* **52–53** 62
[48] Wang F, Feng G B, Zhang X S and Cao M 2016 *Micron* **90** 64
[49] Llacer J and Garwin E L 1969 *J. Appl. Phys.* **40** 2766
[50] Cazaux J 2011 *J. Appl. Phys.* **110** 024906
[51] Cazaux J 2010 *Appl. Surf. Sci.* **257** 1002
[52] Guo J, Wang D and Wen K 2020 *Ceram. Int.* **46** 8352
[53] Zhu X, Guo J and Li X 2021 *Appl. Sci.* **11** 4801
[54] Leenaerts O, Partoens B and Peeters F M 2017 *J. Phys.: Condens. Matter* **29** 035003
[55] Eberlein T, Bangert U and Nair R R 2008 *Phys. Rev. B* **77** 233406
[56] Chaoui Z, Ding Z J and Goto K 2009 *Phys. Rev. A* **373** 1679
[57] Ohta T, Bostwick A and Mcchesney J L 2007 *Phys. Rev. Lett.* **98** 206802